RESEARCH ARTICLE

Check for updates

V2(PO4)O/C@CNT hollow spheres with a core−shell structure as a high performance anode material for lithium-ion batteries†

Bin Xiao, Wen-hai Zhang, Hai-feng Xia, Zhi-teng Wang, Lin-bo Tang, Chang-sheng An, Zhen-jiang He, Hui Tong and Jun-chao Zheng [ID] *

$V_2(PO_4)O$ is a novel promising anode material because of its stable crystal structure, low cost, and environmentally friendliness. However, its low electronic and ionic conductivity result in poor specific capacity and rate performance, hindering its industrial application. In this study, $V_2(PO_4)O/C@CNT$ hollow spheres (HSs) with a core−shell structure were successfully synthesized by a simple spray drying method. Pluronic® F-127 acted as a carbon source and template, and induced the $V_2(PO_4)O$ particles to form HSs. The $V_2(PO_4)O/C@CNT$ HSs were composed of uniform HSs of about 0.4−0.6 μm in diameter and carbon nanotubes (CNTs). The HS structure enhances the electronic conductivity and lithium ion transport rate of $V_2(PO_4)O/C$ materials and thus helps improve the electrochemical performance. CNTs not only increase the electronic conductivity and lithium ion transport rate, but also hinder the aggregation of the HSs. These activities enhance the electrochemical performance. The lithium ion storage behavior of $V_2(PO_4)O/C@CNT$ HSs is systematically studied in the potential range 0.01−3.0V. The $V_2(PO_4)O/C@CNT$ HS anode can achieve a high reversible capacity of 894.9 mA h g^{-1} at 0.1 A g^{-1} and can obtain a reversible capacity of 490.4 mA h g^{-1} at a high rate of 5 A g^{-1}, perhaps the best electrochemical performance demonstrated so far for a $V_2(PO_4)O$ anode material (specific capacity and rate performance), indicating its promise for application as an anode material in advanced lithium-ion batteries.

1. Introduction

With the continuous growth of energy demand, energy storage has become a very important issue. Among the numerous existing energy storage technologies, rechargeable lithium batteries (LIBs) have been extensively applied to portable electronic devices and electric vehicles, owing to their numerous advantages, such as nonexistent memory effect, long cycling life, and high energy density.[1–13] As an important part in the battery, anode materials should be continuously developed and optimized.[14] As far as the charge–discharge mechanism is concerned, anode materials for LIBs can be divided into three types: (i) intercalation type anode materials, such as graphite, Ti,[15] and V-based oxides;[16] (ii) conversion type anode materials, such as transition-metal oxides[17] and transition metal sulfides;[18] and (iii) alloy/de-alloy type anode materials, including Si[19] and Sn.[20] Given the advantages of low cost, outstanding electronic conductivity, and good

chemical/thermal stability, the typical intercalation type anode material graphite has been applied extensively in commercial LIBs. However, the LIBs possess many weaknesses, such as low theoretical capacity (372 mA h g^{-1}) and weak rate property, which hinder the achievement of market demand for high energy density and high power density.[21] Another frequently used commercial anode material, $Li_4Ti_5O_{12}$, has good reversibility, but its low theoretical capacity (175 mA h g^{-1}) and low energy density restrict the material's development.[22] Conversion type anode materials, such as Co_3O_4,[23] MoS_2,[24] and $MoSe_2$,[25] have high capacity and high energy density,[26] but they also have many disadvantages, such as solid electrolyte interphase (SEI) film instability and weak capacity retention. As alloy/de-alloy type anode materials, Si[19] and Sn[20] have high specific capacity. Nevertheless, the large volume expansion in the charge–discharge process hinders their commercial application.[27]

V-based anode materials, for instance Li_3VO_4,[22] VPO_4,[11] and $VOPO_4$,[10] have been widely investigated by researchers. Li_3VO_4, an intercalation type anode material, possesses the advantages of small volume, slight structural changes, and rapid lithium ion diffusion rate. However, the material's low theoretical capacity and weak electronic conductivity hinder its further application. VPO_4 and $VOPO_4$ have stable crystal structures and

School of Metallurgy and Environment, Central South University, Changsha 410083, P. R. China. E-mail: jczheng@csu.edu.cn;
Fax: +86-731-88836357; Tel: +86-731-88836357

high theoretical capacities but poor rate and cycling performances. Nevertheless, even with some weaknesses, V-based anode materials possess enormous potential applications for LIBs due to the various chemical valence states of V.

$V_2(PO_4)O$, as a novel V-based anode material, has attracted attention due to its stable crystal structure, low cost, and environmentally friendliness. The crystal structure of $V_2(PO_4)O$ is composed of $[VO_6]$ octahedra and $[PO_4]$ tetrahedra, and the linking between $[VO_6]$ octahedra is by face contact.[28] The arrays shared by the $[VO_6]$ octahedra with one face can lead to a short V–V distance, which promotes electron hopping between low- and high-valence V sites. The special structure of $V_2(PO_4)O$ equips the material with a relatively high intrinsic electronic conductivity (1.8×10^{-15} S cm^{-1}). The rigid $[PO_4]$ tetrahedra also afford $V_2(PO_4)O$ with excellent structural stability. At present, only one researcher has studied the $V_2(PO_4)O$ material, and a $V_2(PO_4)O/C$ composite was prepared by a hydrothermal method and calcination steps that achieved an appreciable specific capacity of 541 mA h g^{-1} at 0.5 A g^{-1}.[28] However, the obtained $V_2(PO_4)O/C$ composite only delivered a specific capacity of 345.6 mA h g^{-1} at 5 A g^{-1}, which could not meet the needs of industrial applications. And the $V_2(PO_4)O/C$ was composed of nanoscale particles with a particle size between 10 and 30 nm, which can shorten the distance of lithium ion diffusion, but the nanoscale particles had many shortcomings, such as the agglomeration and pulverization of nanoscale particles. This problem may be solved by synthesizing hollow spheres (HSs) of about 0.4–0.6 μm diameter, which can offer a high specific surface area and specific capacity, shorten the lithium ion diffusion path, and provide an enlarged space for volume expansion.[29–31] Meanwhile, the agglomeration of HSs can be inhibited by adding carbon nanotubes (CNTs), which also enhance the electronic conductivity of the $V_2(PO_4)O$ material. In the current study, $V_2(PO_4)O/C@CNT$ HSs were synthesized through a facile spray dryer approach with Pluronic® F-127 acting as a template and carbon (C) source. Pluronic® F-127 can adsorb VO^{3-}, PO_4^{3-}, and NH^{4+}, and then Pluronic® F-127 with absorbed ions was assembled into hollow spheres. The properties of the $V_2(PO_4)O/C@CNT$ HSs were investigated.

2. Experimental

2.1 Material synthesis

NH_4VO_3 (Aladdin >99.9%) and $NH_4H_2PO_4$ (>99.0%) were purchased from Aladdin Co., Ltd. Pluronic® F-127 (Sigma-Aldrich >99.0%) was acquired from Sigma-Aldrich Co., Ltd CNTs (>98%) were obtained from the Chinese Academy of Science, Chengdu Organic Chemistry Co., Ltd. All chemical reagents besides CNTs used in this study were not further purified.

The CNTs used in this study were purified for improving the hydrophilicity of CNTs. 100 mg CNTs was added into 500 mL concentrated HNO_3 solution (68% w/w) and the mixture were sonicated at room temperate for 6 h. After that, the CNTs were washed with deionized water several times and dried by vacuum freeze drying for 16 h.
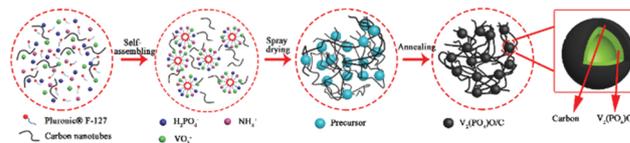

Fig. 1 Schematic diagram of the synthesis process for $V_2(PO_4)O/CNT$ HSs.

$V_2(PO_4)O/C@CNT$ HSs were synthesized by the following steps: NH_4VO_3 (117.0 mg), $NH_4H_2PO_4$ (121.0 mg), and Pluronic® F-127 (1000 mg) were mixed in 100 mL of deionized water under continuous stirring at 80 °C for 2 h. CNTs (100 mg) were added to 100 mL of deionized water and dispersed by ultrasonication for 4 h. Then, the two liquids were mixed, and the resultant solution was dried through a spray dryer with an inlet temperature of 260 °C at a flow rate of 600 mL h^{-1}. Finally, the $V_2(PO_4)O/C@CNT$ precursor was heated at 850 °C for 10 h under a 10% H_2/Ar atmosphere to acquire $V_2(PO_4)O/C@CNT$ HSs. By contrast, $V_2(PO_4)O/C$ HSs were fabricated by the same steps without CNTs. The process of preparing $V_2(PO_4)O/C@CNT$ HSs is shown in Fig. 1.

2.2 Material characterization

Cu Kα radiation X-ray diffraction (XRD, Rint-2000, Rigaku) was applied to test the structural and crystalline phase analyses of the as-prepared samples. A simultaneous thermal analyzer (STA 449F3, NETZSCH, Germany) was used to measure the C content of the as-prepared samples at a heating rate of 5 °C min^{-1} at an air flow of 100 mL min^{-1}. The Brunauer–Emmett–Teller (BET) method was employed to examine the specific surface area through a micromeritics surface area and porosity analyzer (ASAP 2020 HD88, USA). An Invia Raman spectrometer was employed to examine the Raman spectra of both samples. An IRAffinity-1 FTIR spectrometer (SHIMADZU) was applied to obtain Fourier transform infrared (FTIR) spectra. The morphology of the as-synthesized samples was obtained by field-emission scanning electron microscopy (FESEM; JEOL, JSM-7001F) coupled with energy-dispersive X-ray spectroscopy (EDX) and transmission electron microscopy (TEM; JEOL, JEM-3000F). X-ray photoelectron spectroscopy (XPS; VG ESCALAB MK II) was used to test the surface chemical valences of both samples.

2.3 Electrochemical measurements

The electrochemical characterization of $V_2(PO_4)O/C@CNT$ HSs and $V_2(PO_4)O/C$ HSs was examined by a coin-type cell (CR2025). The typical electrode loading was in the range of 3–3.5 mg cm^{-2}. The working electrodes in the coin-type cell were prepared through the following steps. The active materials, polyvinylidene fluoride adhesive, and acetylene black were mixed at a mass ratio of 7 : 1 : 2. Then, a finite amount of N-methyl-2-pyrrolidone (NMP) was dropped into the above mixture; after grinding, the slurry was cast onto a Cu foil. The coated Cu foil was placed in a vacuum drying oven at 120 °C for 8 h and punched into disks with diameters of 12 mm. A glove box under dry Ar was applied to assemble the coin-type cell, in which the Cu foil acted as the counter electrode and the polypropylene film served as the separator.

This journal is © The Royal Society of Chemistry and the Chinese Chemical Society 2019

Mater. Chem. Front., 2019, 3, 456–463 | 457

The electrolyte used in the coin-type cell was 1 mol L^{-1} $LiPF_6$ dissolved in a 1:1 volume mixture of ethylene carbonate/dimethyl carbonate. The rate and cycling performances of the cells were examined by a LAND battery cycler between 0.01 and 3.0 V *versus* Li/Li^+ at 25 °C. A CHI660D electrochemical analyzer (Shanghai, Chenhua) was applied to achieve cyclic voltammograms in the potential range of 0.01–3.0 V and electrochemical impedance spectroscopy (EIS) between 0.1 Hz and 100.00 kHz at 25 °C.

3. Results and discussion

The preparation of the $V_2(PO_4)O/C@CNT$ HS composite involves two steps. At first, a suspension solution containing VO^{3-}, PO_4^{3-}, NH^{4+}, Pluronic® F-127 and CNTs was dried by spray drying, and the $V_2(PO_4)O/C@CNT$ HS precursor was obtained. Pluronic® F-127 is an amphiphilic triblock copolymer, which can form macromolecule micelles consisting of a hydrophilic shell and lipophilic core after dissolving in water.[32] After the formation of spherical micelle templates, the ions of VO^{3-}, PO_4^{3-}, and NH^{4+} were adsorbed on the surface of the templates. During the annealing process, Pluronic® F-127 ($H(OCH_2CH_2)_x(OCH_2CHCH_3)_y(OCH_2CH_2)_2OH$) and NH_4VO_3 reacted with $NH_4H_2PO_4$ in a high temperature environment (850 °C, 10 hours) to form $V_2(PO_4)O$ and carbon. The reaction equation for this process should be written as the following:

$$NH_4VO_3 + NH_4H_2PO_4 + H(OCH_2CH_2)_x(OCH_2CHCH_3)_y$$

$$(OCH_2CH_2)_2OH \rightarrow V_2(PO_4)O + H_2O + C + CO + CO_2 + NH_3.$$

The process of synthesizing $V_2(PO_4)O/C$ HSs is shown in Fig. 1.

The crystallographic structure of the synthesized $V_2(PO_4)O/C@CNT$ HSs and $V_2(PO_4)O/C$ HS composite was examined through XRD (Fig. 2). As shown in the XRD patterns (Fig. 2a), the $V_2(PO_4)O/C@CNT$ HSs and $V_2(PO_4)O/C$ HS composite were well indexed to the tetragonal structure (space group $I4_1/amd$ (141), $a = 5.362$ Å, $b = 5.362$ Å, $c = 12.378$ Å; JCPDS No. 83-0585), which indicates the high crystallinity and purity of $V_2(PO_4)O$.[28] Comparing the XRD results of the CNTs and $V_2(PO_4)O/C@CNT$ HS composite, we showed the CNT diffraction peak in the XRD of $V_2(PO_4)O/C@CNT$ HSs. This finding suggests the existence of CNTs in the $V_2(PO_4)O/C@CNT$ HS composite. The C content of the $V_2(PO_4)O/C@CNT$ HSs and $V_2(PO_4)O/C$ HS composite was tested by thermogravimetric analysis (Fig. 2b) tested with a heating rate of 5 °C min^{-1} under an air flow of 100 mL min^{-1}. The weight of $V_2(PO_4)O/C@CNT$ HSs and $V_2(PO_4)O/C$ HSs decreased between 400 °C and 570 °C because of C oxidation reaction. The weight loss of the $V_2(PO_4)O/C$ HS composite was estimated to be 31.79%, and that of the $V_2(PO_4)O/C@CNT$ HS composite was 36.36%. These values suggest that the CNT content of the $V_2(PO_4)O/C@CNT$ HS composite was approximately equal to 4.57%.

To characterize the porosity properties of the $V_2(PO_4)O/C@CNT$ HSs and $V_2(PO_4)O/C$ HS composite, N_2 absorption–desorption isotherms were examined. In Fig. 2c, the specific surface area of the $V_2(PO_4)O/C@CNT$ HS composite was 59.398 m^2 g^{-1}, which was higher than that of the $V_2(PO_4)O/C$
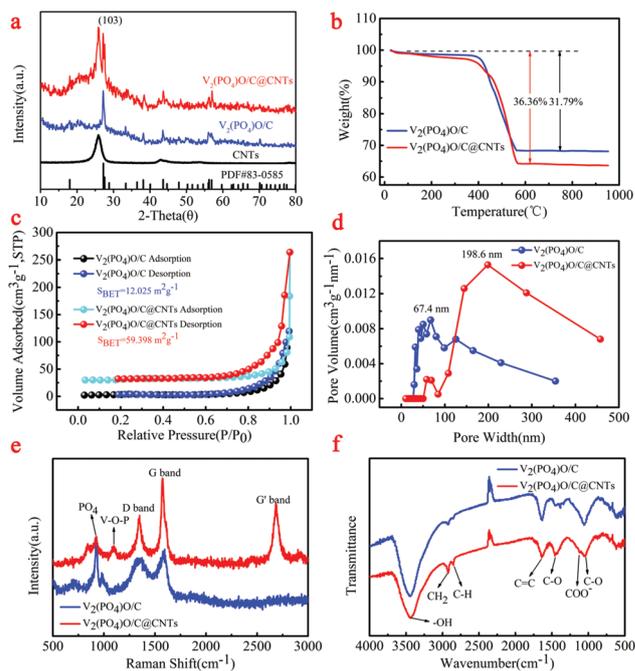
Fig. 2 (a) XRD of $V_2(PO_4)O/CNT$ HSs and $V_2(PO_4)O/C$ HSs; (b) TG curves of $V_2(PO_4)O/CNT$ HSs and $V_2(PO_4)O/C$ HSs; (c) N_2 adsorption–desorption isotherms of $V_2(PO_4)O/CNT$ HSs and $V_2(PO_4)O/C$ HSs; (d) corresponding pore size distribution performed by the BJH method; (e) Raman spectrum of $V_2(PO_4)O/CNT$ HSs and $V_2(PO_4)O/C$ HSs; (f) FTIR of $V_2(PO_4)O/CNT$ HSs and $V_2(PO_4)O/C$ HSs.

HS composite (12.025 m^2 g^{-1}). Such an augmented specific surface area for the $V_2(PO_4)O/C@CNT$ HS composite increased the area of contact between the active material and the electrolyte. This expanded area helped shorten the lithium diffusion distance. The pore size distributions of the $V_2(PO_4)O/C@CNT$ HSs and $V_2(PO_4)O/C$ HSs were calculated from the desorption branch (Fig. 2d). The pore size distribution of the $V_2(PO_4)O/C@CNT$ HSs was in the range of 58.3–457.5 nm, and a wide peak was located at about 198.6 nm. Meanwhile, the pore size distribution of the $V_2(PO_4)O/C$ HSs was in the range of 29.5–354.3 nm, and a wide peak was located at about 67.4 nm. Voids in the particle not only provide access to electrolyte but also provide space for material volume expansion. Both factors can improve effectively the long cycling stability of materials.

The Raman spectra of the $V_2(PO_4)O/C@CNT$ HSs and $V_2(PO_4)O/C$ HSs are shown in Fig. 2e. Two strong peaks are located at 1347 and 1575 cm^{-1} in the spectra of both samples; these peaks are assigned to the disorder-induced phonon (D band) and G-line tangential modes (G band), respectively, of C materials.[33] A strong peak also situated at 2686 cm^{-1} in the spectrum of the $V_2(PO_4)O/C@CNT$ HSs corresponds to the G' mode (G' band) of the CNTs. Another two peaks at 925 and 1093 cm^{-1} in the spectrum of the $V_2(PO_4)O/C@CNT$ HSs are indexed to the totally symmetric PO_4 "breathing" vibration and the V–O–P stretch, respectively.[34] To obtain further information on both samples, we performed FTIR spectroscopy in Fig. 2f. Three peaks were observed at 3439, 2925, and 2849 cm^{-1} at 2500–3500 cm^{-1} and assigned to the –OH mode and CH_2 and
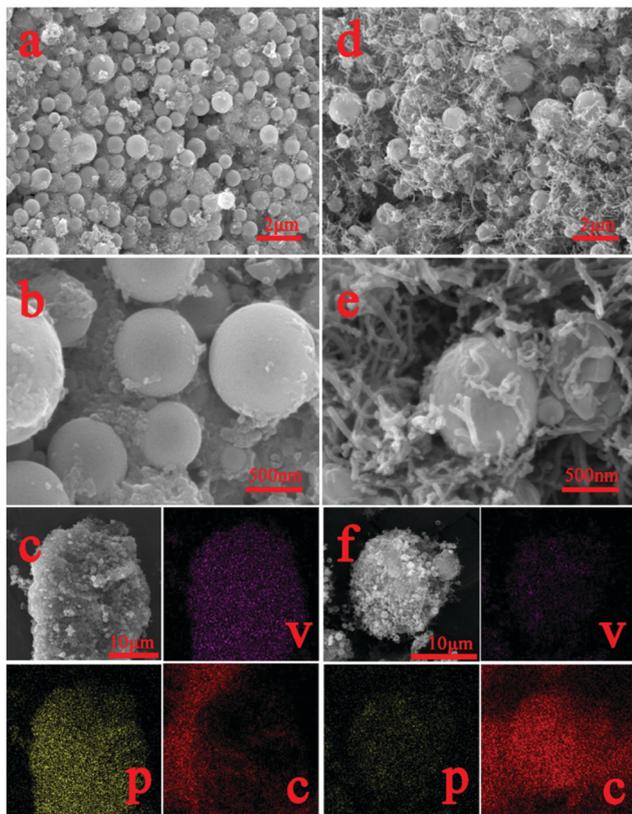
Fig. 3 (a and b) SEM images of $V_2(PO_4)O/C$ HSs; (d and e) SEM images of $V_2(PO_4)O/C@CNT$ HSs; (c) EDX elemental mapping of $V_2(PO_4)O/C$ HSs; (d) EDX elemental mapping of $V_2(PO_4)O/C@CNT$ HSs.

C–H bands, respectively.[35–37] In addition, the signals at 1634, 1448, 1388, and 1055 cm^{-1} can be assigned to the C=C groups, C=O band, COO– groups, and C–O band, respectively.[38]

To observe the morphology of the as-synthesized samples, we conducted FESEM (Fig. 3). Clearly, the as-synthesized $V_2(PO_4)O/C@CNT$ HSs and $V_2(PO_4)O/C$ HSs were composed of uniform spheres of 0.4–0.6 μm diameter (Fig. 3a, b, d, and e). The agglomeration phenomenon of $V_2(PO_4)O/C$ spheres appeared in the $V_2(PO_4)O/C$ HS samples. However, $V_2(PO_4)O/C$ spheres in the $V_2(PO_4)O/C@CNT$ HS sample were uniformly dispersed in the CNT network and became beneficial for improving the specific surface area of the $V_2(PO_4)O/C@CNT$ HS sample. Enlarging the FESEM image of the $V_2(PO_4)O/C@CNT$ HS sample, it can be observed that some CNTs penetrated into the $V_2(PO_4)O/C@CNT$ HSs in Fig. S3 (ESI†), which can be proved by the following TEM image. Improving specific surface area of the $V_2(PO_4)O/C@CNT$ HS sample can increase the contact area between the active material and the electrolyte, which is in favor of shortening the lithium diffusion distance.[39,40] This CNT network can efficiently increase the electron transport rate between the $V_2(PO_4)O/C$ spheres, thereby improving the electronic conductivity of $V_2(PO_4)O/C@CNT$ spheres. The results can be proved by the following EIS findings. The high specific surface area and enhanced electronic conductivity of the $V_2(PO_4)O/C@CNT$ spheres are beneficial for enhancing the electrochemical performances of $V_2(PO_4)O/C$, especially the

rate capability and long cycle performance. To clarify the spatial distribution of V, phosphorus (P), and C in the $V_2(PO_4)O/C$ HSs and $V_2(PO_4)O/C@CNT$ HSs, we performed EDX elemental mapping. The mapping images in Fig. 3c and f demonstrate that the V, P, and C elements in both samples are distributed uniformly on the surface and suggest the presence of a thin C layer on the surface of the $V_2(PO_4)O/C$ spheres. This phenomenon can be observed in the following TEM images.

To illustrate the internal structure of the as-prepared samples, we examined high-magnification TEM and high-resolution TEM (HRTEM) images. As shown in Fig. 4a and b, the $V_2(PO_4)O/C$ spheres were hollow structures, and the diameters of both samples lay within 0.4–0.6 nm, which matched the result of the SEM images. The $V_2(PO_4)O/C$ spheres in the $V_2(PO_4)O/C@CNT$ HS sample were wrapped with CNTs. Furthermore, a uniform C-coating layer was present on the surface of the
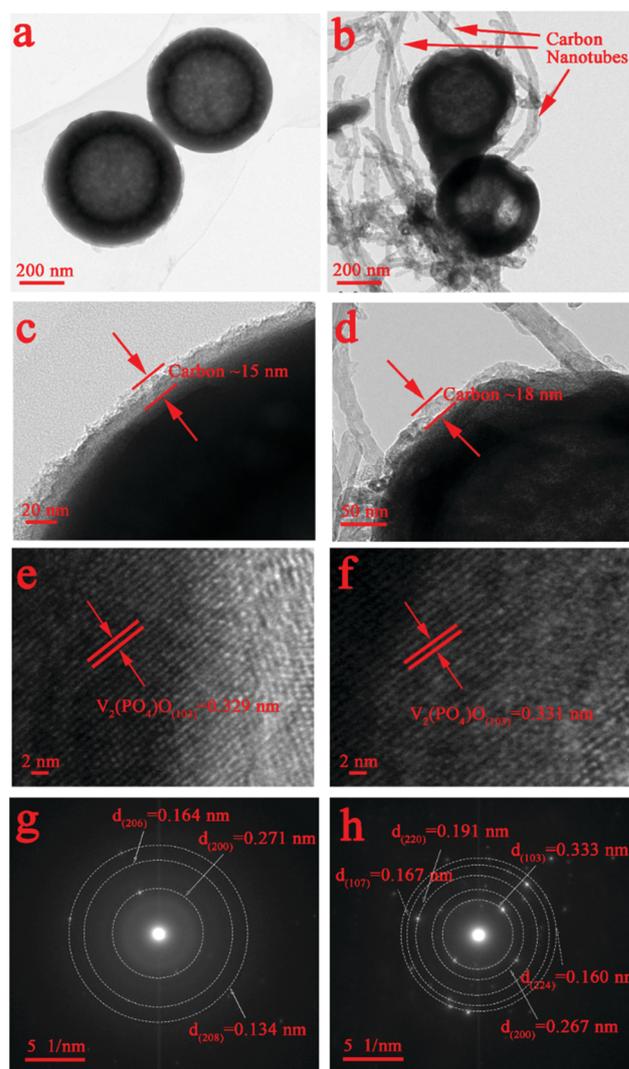
Fig. 4 (a and c) TEM images of $V_2(PO_4)O/C$ HSs; (b and d) TEM images of $V_2(PO_4)O/C@CNT$ HSs; (e) HRTEM image of $V_2(PO_4)O/C$ HSs; (f) HRTEM image of $V_2(PO_4)O/C@CNT$ HSs; (g) SAED patterns of $V_2(PO_4)O/C$ HSs; (h) SAED patterns of $V_2(PO_4)O/C@CNT$ HSs.

nanoparticles forming a core–shell structure, and the thickness of the C layer was about ~18 nm. As shown in the TEM image at low magnification, it can be clearly observed that a complete spherical carbon shell coated the $V_2(PO_4)O/C$ sphere in Fig. S2 (ESI†). The carbon shell not only promotes the electron transfer but also inhibits the volume expansion of the $V_2(PO_4)O$ spheres in the charge–discharge process. In addition, it can be seen that CNTs are not simply attached to the surface of $V_2(PO_4)O/C$ HSs, but penetrated into them, as shown in Fig. S4 (ESI†). Clear lattice fringes are displayed in the HRTEM images in Fig. 4e and f. The observed interplane spaces were 0.329 and 0.331 nm, which were well indexed to the (103) plane of tetragonal $V_2(PO_4)O$ (JCPDS No. 83-0585). The selected area electron diffraction patterns of the $V_2(PO_4)O/C@CNT$ HSs and $V_2(PO_4)O/C$ HSs are shown in Fig. 4g and h, which can be indexed to the tetragonal structure of $V_2(PO_4)O$ (JCPDS No. 83-0585). The diffraction rings in Fig. 4g can be indexed to (200), (206), and (208), and those in Fig. 4h can be indexed to (103), (200), (220), (107), and (224), respectively.

To confirm the surface chemical valences of both samples, we conducted XPS. Indeed, the survey spectra (Fig. S1a and b, ESI†) of the $V_2(PO_4)O/C@CNT$ HS and $V_2(PO_4)O/C$ HS samples clearly revealed the existence of the V, P, O, and C elements. This result agreed with the above EDX elemental mapping results. As shown in Fig. 5a, the binding energy centered at 517.0 and 524.5 eV in the V 2p spectrum of $V_2(PO_4)O/C@CNT$ HSs can be attributed to V $2p_{3/2}$ and V $2p_{1/2}$ of V^{2+} and V^{3+}, which were different from that of the $V_2(PO_4)O/C$ HSs. The V 2p spectrum of the $V_2(PO_4)O/C$ HSs can be indexed to V $2p_{3/2}$ and V $2p_{1/2}$ and confirms the tervalence of V (Fig. S1c, ESI†). The V $2p_{3/2}$ peak of the $V_2(PO_4)O/C$ HS sample deconvoluted into three subpeaks centered at 516, 517.2, and 517.5 eV (Fig. S1c, ESI†), which correspond to V^{4+}, V^{3+}, and V^{5+}, respectively. Due to the poor air tightness of the furnace, there may be air entering the furnace in the annealing process. In the synthetic reaction of $V_2(PO_4)O$, water was formed at high temperature. CNTs reacted with water and produced CO and H_2; the reaction equation for this process was the following:

$C + H_2O \rightarrow CO + H_2$. CO and H_2 both are reductive gases, which can avoid vanadium oxidation. The P 2p XPS spectrum of the $V_2(PO_4)O/C@CNT$ HSs in Fig. 5b can be fitted to three subpeaks centered at 132.8, 133.5, and 134.4 eV, which correspond to P–C, P–O, and P–O bonds, respectively, whereas that of $V_2(PO_4)O/C$ HSs (Fig. S1d, ESI†) was divided into two components assigned to the P–O bond (133.1 and 133.8 eV).[34] The O 1s spectrum of $V_2(PO_4)O/C@CNT$ HSs in Fig. 5c was divided into two subpeaks corresponding to the P–O (134.0 eV) and C–O (133.1 eV) bonds, respectively, whereas that of $V_2(PO_4)O/C$ HSs was split into four peaks (Fig. S1e, ESI†) corresponding to V–O (530.2 and 531.4 eV), P–O (531.4 and 532 eV), and C–O (533 eV), respectively. Furthermore, the P–C bond (285.1 eV) was further proved by the C 1s spectrum of $V_2(PO_4)O/C@CNT$ HSs (Fig. 5d), which cannot be found in the C 1s spectrum of $V_2(PO_4)O/C$ HSs. The reason for the formation of the P–C bond may be the high-temperature reaction between CNTs and $(NH_4)H_2PO_4$, thereby demonstrating that the $V_2(PO_4)O/C$ HSs are chemically bonded to the CNTs *via* P–C bonds. The results revealed the successful improvement of electrical conductivity of the materials and alleviation of the volume expansion. The other two divided peaks of $V_2(PO_4)O/C@CNT$ HSs at 284.7 and 286 eV were assigned to the C–O bond, whereas those of $V_2(PO_4)O/C$ HSs (Fig. S1f, ESI†) were fitted to C–O (284.7 and 286.2 eV) and C–C (285.7 eV), respectively.

The electrochemical performances of $V_2(PO_4)O/C@CNT$ HSs and $V_2(PO_4)O/C$ HSs as LIB anodes were tested. The cyclic voltammetry (CV) curves of the $V_2(PO_4)O/C@CNT$ HS composite are shown in Fig. 6a when these were tested in the potential range 0.01–3.0 V at a scanning rate of 0.1 mV s^{-1}. The charge–discharge curves of the $V_2(PO_4)O/C@CNT$ HS and $V_2(PO_4)O/C$ HS samples at various rates, from 0.1 A g^{-1} to 5.0 A g^{-1} between 0.01 and 3.00 V, are shown in Fig. 6b and c, respectively. We observed the existence of three reduction peaks located at 0.77, 1.7, and 2.52 V and two oxidation peaks at 1.8 and 2.65 V in the first cycle of the CV curves (Fig. 6a). The obvious reduction peak centered at 0.77 V in the first cathodic cycle that disappeared in the following cycles was assigned to the formation of an SEI layer, which corresponded to the plateau at 0.77 V of the first discharge curves of the $V_2(PO_4)O/C@CNT$ HS sample in Fig. 6b. The other two reduction peaks at 1.7 and 2.52 V were assigned to the insertion reaction between $V_2(PO_4)O$ and Li^+. In the anodic process of the first cycle, the two oxidation peaks at 1.8 and 2.65 V were attributed to the Li^+ deintercalation reaction. In the following two cycles, the CV curves of the $V_2(PO_4)O/C@CNT$ HS composite maintain high coincidence and demonstrate the stability of the electrochemical reaction.

In the discharge/charge profiles of the $V_2(PO_4)O/C@CNT$ HS sample (Fig. 6b), two pairs of weak discharge/charge plateaus of 1.7/1.8 V and 2.52/2.65 V in the first cycle at 0.1 A g^{-1} between 0.01 and 3.00 V were assigned to the related peaks of CV curves. The $V_2(PO_4)O/C@CNT$ HS sample can achieve a discharge capacity of 1476.7 mA h g^{-1} and a charge capacity of 846.9 mA h g^{-1}, whereas the coulombic efficiency was 57.35%. With regards the rate performance, the $V_2(PO_4)O/C@CNT$ HS sample can achieve a high reversible capacity of 894.9, 689.8, 650.4, 602.6, 565.8, and
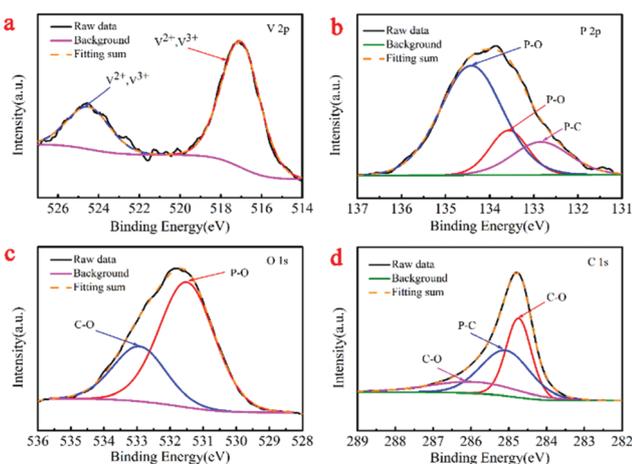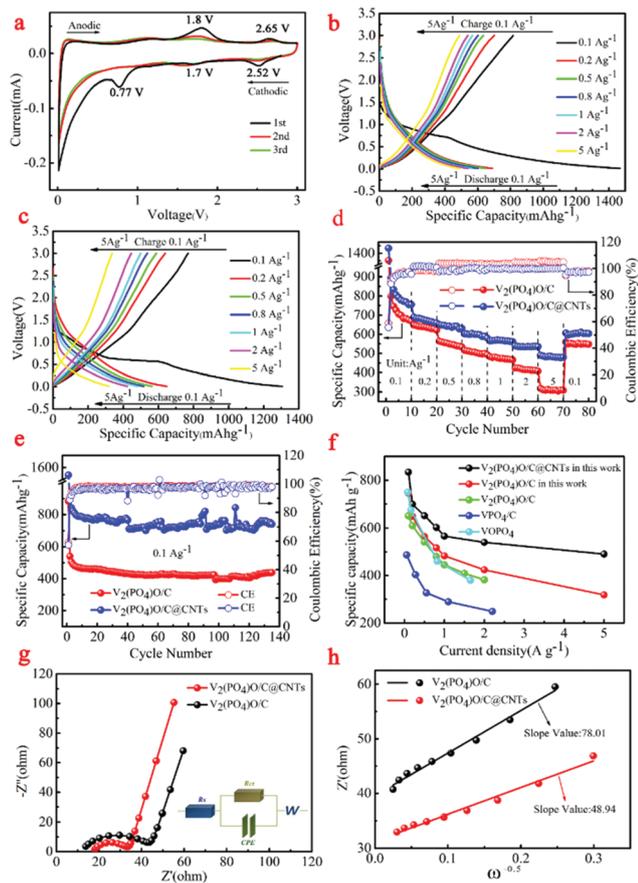

Fig. 5 (a) XPS core level of V 2p in $V_2(PO_4)O/C@CNT$ HSs; (b) XPS core level of P 2p in $V_2(PO_4)O/C@CNT$ HSs; (c) XPS core level of O 1s in $V_2(PO_4)O/C@CNT$ HSs; (d) XPS core level of C 1s in $V_2(PO_4)O/C@CNT$ HSs.

460 | *Mater. Chem. Front.*, 2019, **3**, 456–463

This journal is © The Royal Society of Chemistry and the Chinese Chemical Society 2019

Fig. 6 (a) The CV curves of $V_2(PO_4)O/C@CNT$ HSs; (b) the first charge–discharge profiles of the $V_2(PO_4)O/C@CNT$ HS sample from 0.1 to 5.0 A g^{-1}; (c) the first charge–discharge profiles of the $V_2(PO_4)O/C$ HS sample from 0.1 to 5.0 A g^{-1}; (d) rate performance of $V_2(PO_4)O/C@CNT$ HSs and $V_2(PO_4)O/C$ HSs; (e) cycling performance of $V_2(PO_4)O/C@CNT$ HSs and $V_2(PO_4)O/C$ HSs; (f) the rate performance of $V_2(PO_4)O/C@CNT$ HSs compared to other materials ($V_2(PO_4)O/C$,[28] VPO_4/C,[5] $VOPO_4$[10]); (g) the Nyquist plots and the corresponding fitted curves of V $V_2(PO_4)O/C@CNT$ HSs and $V_2(PO_4)O/C$ HSs; (h) plots showing the relationship between Z' and $\omega^{-0.5}$ at low frequencies, calculated from the EIS data.

539.9 mA h g^{-1} at the different current densities of 0.1, 0.2, 0.5, 0.8, 1.0, and 2.0 A g^{-1}, respectively, which are all higher than that of the $V_2(PO_4)O/C$ HS sample at various densities (Fig. 6c and d). In particular, the sample can even obtain a reversible capacity of 490.4 mA h g^{-1} at the high rate of 5.0 A g^{-1}. When the current density returns to 0.1 A g^{-1}, it achieved a reversible capacity of 606.9 mA h g^{-1} with a capacity retention of 97.4% (Fig. 6d), which suggested satisfactory rate tolerance of the $V_2(PO_4)O/C@CNT$ HS sample. Moreover, the long-term cycling performances of the $V_2(PO_4)O/C@CNT$ HSs and $V_2(PO_4)O/C$ HSs are shown in Fig. 6e. The $V_2(PO_4)O/C@CNT$ HS sample delivered a reversible capacity of 741.5 mA h g^{-1} after 135 cycles at 0.1 A g^{-1}, which was higher than that of the $V_2(PO_4)O/C$ HS sample. Compared with other anode materials, the rate performance of the $V_2(PO_4)O/C@CNT$ HS sample was much better.[28] The major causes of this result were the higher theoretical specific capacity, higher electronic conductivity, and good Li$^+$ ion coefficient.

To determine the source of the good electrochemical properties, we examined the EIS results in the range of 0.1 Hz to 100 kHz (Fig. 6g). To simulate Nyquist plots, we adopted a simplified equivalent circuit (Fig. 6g). The first intercept of the semicircle at the Z' axis in the high-frequency region in Fig. 6g was relevant to the resistance R_s, which was the combined Ohmic resistance of the separator, electrolyte, and metal electrode. The charge transfer resistance was represented by R_{ct}, which corresponded to the distance between the two intercepts of the semicircle on the Z' axis. The fitting results of the Nyquist plots for both samples are listed in Table 1. The R_s values of the $V_2(PO_4)O/C@CNT$ HSs and $V_2(PO_4)O/C$ HSs were 17.37 and 11.74 Ω, respectively, which were higher than that of the $V_2(PO_4)O/C$ HSs in the literature.[28] However, the R_{ct} of the $V_2(PO_4)O/C@CNT$ HSs was 13.5 Ω, which was far lower than that of the $V_2(PO_4)O/C$ HSs (29.47 Ω); this result suggested that CNTs reduced the charge resistance and improve electronic conductivity. Moreover, the R_{ct} values of both samples were lower than those of the literature and indicated that the HS structure was conducive to the transmission of electrons.[28] The electrochemical reaction is dominated by ion diffusion when a threshold of the electronic conductivity is exceeded. The lithium ion diffusion coefficient D_{Li^+} was calculated using EIS data on the basis of the following equations:[41]

$$D_{Li^+} = \frac{R^2 T^2}{2A^2 n^4 F^4 C^2 \sigma_\omega^2} \qquad (1)$$

$$Z' = R_e + R_{ct} + \sigma_\omega \omega^{-0.5} \qquad (2)$$

where R represents the gas constant, T represents the absolute temperature, F represents the Faraday constant, n represents the number of electrons transferred per molecule, A represents the active surface area of the electrode (0.50 cm^2), C_0 represents the concentration of lithium ions in the electrolyte (1×10^{-3} mol cm^{-3}), D_{Li^+} is the apparent ion diffusion coefficient, and E_q is the Warburg factor related to Z' and can be achieved by the slope of the fitting line of EIS data at low frequencies in Fig. 6h. The calculated results of D_{Li^+} at low frequencies are listed in Table 1. The D_{Li^+} of the $V_2(PO_4)O/C@CNT$ HSs was 1.85×10^{-14} cm^2 s^{-1}, which is higher than that of the $V_2(PO_4)O/C$ HSs (7.28×10^{-15} cm^2 s^{-1}). As can be seen from above, CNTs hindered the aggregation of the HSs, which can shorten the path of lithium ion diffusion. In addition, in Fig. S3 and S4 (ESI†), it was obtained that CNTs are not simply attached to the surface of $V_2(PO_4)O/C$ HSs, but penetrated into them, which can also provide more channels for lithium ions to enter the interior of the particles. All of this can accelerate the lithium ion transport rate. Compared with the D_{Li^+} of the $V_2(PO_4)O/C$ materials in the literature,[28] those of both samples remained higher and suggest that the HS structure is beneficial for the transmission of lithium

Table 1 The value of R_s, R_{ct}, slope values and D_{Li^+} of $V_2(PO_4)O/C$ HSs, $V_2(PO_4)O/C@CNT$ HSs and $V_2(PO_4)O/C$

Sample	R_s (Ω)	R_{ct} (Ω)	Slope value	D_{Li^+} (cm^2 s^{-1})
$V_2(PO_4)O/C$	11.74	29.47	78.01	7.28×10^{-15}
$V_2(PO_4)O/C@CNTs$	17.37	13.5	48.94	1.85×10^{-14}
$V_2(PO_4)O/C$[28]	3	48	198.6	5.75×10^{-15}

This journal is © The Royal Society of Chemistry and the Chinese Chemical Society 2019

Mater. Chem. Front., 2019, **3**, 456–463 | **461**

ions. The high electronic conductivity and lithium ion transport rate of the $V_2(PO_4)O/C@CNT$ HSs can enhance the rate performance and cycling performance of the material, as indicated by the preceding results.

4. Conclusions

In summary, $V_2(PO_4)O/C@CNT$ HSs with a core–shell structure were successfully synthesized *via* a facile spray drying method. The $V_2(PO_4)O/C@CNT$ HS composite exhibited a high specific capacity and good rate performance. The $V_2(PO_4)O/C@CNT$ HSs delivered a high reversible capacity of 894.9, 689.8, 650.4, 602.6, 565.8, and 539.9 mA h g^{-1} at the current densities of 0.1, 0.2, 0.5, 0.8, 1.0, and 2.0 A g^{-1}, respectively. In particular, the $V_2(PO_4)O/C@CNT$ HSs obtained a reversible capacity of 490.4 mA h g^{-1} at the high rate of 5.0 A g^{-1}. The good electrochemical performances of the $V_2(PO_4)O/C@CNT$ HSs benefitted from the material's unique HS structure, which enhanced the electronic conductivity and lithium ion transport rate of the $V_2(PO_4)O/C$ HS materials. The CNTs also played an important role in this enhancement. The addition not only increased the electronic conductivity and lithium ion transport rate but also hindered the aggregation of the HSs. Thus, the $V_2(PO_4)O/C@CNT$ HSs, as a potential novel anode material can be used in advanced lithium ion batteries in the future.

Conflicts of interest

There are no conflicts to declare.

Acknowledgements

Notes and references

1 C. Shen, B. Zhang, J. F. Zhang, J. C. Zheng, Y. D. Han and H. Li, *RSC Adv.*, 2015, **5**, 7208–7214.

2 J. C. Zheng, Y. D. Han, B. Zhang, C. Shen, L. Ming and J. F. Zhang, *RSC Adv.*, 2014, **4**, 41076–41080.

3 J. C. Zheng, Y. D. Han, B. Zhang, C. Shen, L. Ming and J. F. Zhang, *ACS Appl. Mater. Interfaces*, 2014, **6**, 13520–13526.

4 C. Shen, J. C. Zheng, B. Zhang, Y. D. Han, J. F. Zhang, L. Ming, H. Li and X. B. Yuan, *RSC Adv.*, 2014, **4**, 40912–40916.

5 J. C. Zheng, Y. D. Han, B. Zhang, C. Shen, L. Ming, X. Ou and J. F. Zhang, *ACS Appl. Mater. Interfaces*, 2014, **6**, 6223–6226.

6 J. C. Zheng, Y. D. Han, D. Sun, B. Zhang and E. J. Cairns, *Energy Storage Mater.*, 2017, **7**, 48–55.

7 B. Xiao, B. Zhang, J. C. Zheng, L. B. Tang, C. S. An, Z. J. He, H. Tong and W. J. Yu, *Ceram. Int.*, 2018, **44**, 13113–13121.

8 B. Zhang, Y. D. Han, J. C. Zheng, C. Shen, L. Ming and J. F. Zhang, *J. Power Sources*, 2014, **264**, 123–127.

9 B. Xiao, B. Zhang, L. B. Tang, C. S. An, Z. J. He, H. Tong, W. J. Yu and J. C. Zheng, *Ceram. Int.*, 2018, **44**, 15044–15049.

10 B. Zhang, Y. D. Han, J. C. Zheng, J. F. Zhang, C. Shen, L. Ming, X. B. Yuan and H. Li, *Chem. Commun.*, 2014, **50**, 11132–11134.

11 L. B. Tang, B. Xiao, C. S. An, H. Li, Z. J. He and J. C. Zheng, *Ceram. Int.*, 2018, **44**, 14432–14438.

12 H. Chen, M. Ling, L. Hencz, H. Y. Ling, G. Li, Z. Lin, G. Liu and S. Zhang, *Chem. Rev.*, 2018, **118**, 8936–8982.

13 D. Adekoya, X. Gu, M. Rudge, W. Wen, C. Lai, M. Hankel and S. Zhang, *Adv. Funct. Mater.*, 2018, 1803972, DOI: 10.1002/adfm.201803972.

14 M. Zhang, T. Wang and G. Cao, *Int. Mater. Rev.*, 2015, **60**, 330–352.

15 L. Shen, E. Uchaker, X. Zhang and G. Cao, *Adv. Mater.*, 2012, **24**, 6502–6506.

16 X. Wang, Y. Huang, D. Jia, W. K. Pang, Z. Guo, Y. Du, X. Tang and Y. Cao, *Inorg. Chem.*, 2015, **54**, 11799–11806.

17 M. Liu, C. Yan and Y. Zhang, *Sci. Rep.*, 2015, **5**, 8326.

18 L. Zhang, Q. Wei, D. Sun, N. Li, H. Ju, J. Feng, J. Zhu, L. Mai, E. J. Cairns and J. Guo, *Nano Energy*, 2018, **51**, 391–399.

19 N. Liu, Z. Lu, J. Zhao, M. T. McDowell, H. W. Lee, W. Zhao and Y. Cui, *Nat. Nanotechnol.*, 2014, **9**, 187–192.

20 Y. Xu, Q. Liu, Y. Zhu, Y. Liu, A. Langrock, M. R. Zachariah and C. Wang, *Nano Lett.*, 2013, **13**, 470–474.

21 D. Kong, H. He, Q. Song, B. Wang, W. Lv, Q.-H. Yang and L. Zhi, *Energy Environ. Sci.*, 2014, 7, 3320–3325.

22 C. Zhang, H. Song, C. Liu, Y. Liu, C. Zhang, X. Nan and G. Cao, *Adv. Funct. Mater.*, 2015, **25**, 3497–3504.

23 J. Liu, H. Xia, L. Lu and D. Xue, *J. Mater. Chem.*, 2010, **20**, 1506.

24 K. Chang, W. Chen, L. Ma, H. Li, H. Li, F. Huang, Z. Xu, Q. Zhang and J. Y. Lee, *J. Mater. Chem.*, 2011, **21**, 6251.

25 Y. Liu, M. Zhu and D. Chen, *J. Mater. Chem. A*, 2015, **3**, 11857–11862.

26 J. Liu and D. Xue, *Nanoscale Res. Lett.*, 2010, **5**, 1525–1534.

27 M. Holzapfel, H. Buqa, W. Scheifele, P. Novak and F. M. Petrat, *Chem. Commun.*, 2005, 1566–1568, DOI: 10.1039/b417492e.

28 X. Nan, C. Liu, C. Zhang, W. Ma, K. Wang, Z. Li and G. Cao, *J. Mater. Chem. A*, 2016, **4**, 9789–9796.

29 D. Mao, J. Wan, J. Wang and D. Wang, *Adv. Mater.*, 2018, e1802874, DOI: 10.1002/adma.201802874.

30 J. Wang, Y. Cui and D. Wang, *Adv. Mater.*, 2018, e1801993, DOI: 10.1002/adma.201801993.

31 J. Qi, X. Lai, J. Wang, H. Tang, H. Ren, Y. Yang, Q. Jin, L. Zhang, R. Yu, G. Ma, Z. Su, H. Zhao and D. Wang, *Chem. Soc. Rev.*, 2015, **44**, 6749–6773.

32 C. M. Papadakis, R. Ivanova, K. Lüdtke, K. Mortensen, P. K. Pranzas and R. Jordan, *J. Appl. Crystallogr.*, 2010, **40**, s361–s362.

33 L. Tzounis, S. Debnath, S. Rooj, D. Fischer, E. Mäder, A. Das, M. Stamm and G. Heinrich, *Mater. Des.*, 2014, **58**, 1–11.

34 D. Zhao, T. Meng, J. Qin, W. Wang, Z. Yin and M. Cao, *ACS Appl. Mater. Interfaces*, 2017, **9**, 1437–1445.

35 D. Kumar, G. Kumar and V. Agrawal, *Parasitol. Res.*, 2018, **117**, 377–389.

36 O. Carnevali, C. Conti, P. Ferraris, M. G. Garavaglia, G. Gioacchini, E. Giorgini, C. Rubini, S. Sabbatini and G. Tosi, *J. Mol. Struct.*, 2009, **938**, 207–213.

37 S. Orefuwa, M. E. Naggar, I. Shehadi, M. M. Chehimi and A. A. Mohamed, *J. Nanosci. Nanotechnol.*, 2017, **17**, 4063–4068.

38 J. T. Kloprogge, L. Hickey and R. L. Frost, *J. Raman Spectrosc.*, 2004, **35**, 967–974.

39 J. Wang, H. Tang, H. Wang, R. Yu and D. Wang, *Mater. Chem. Front.*, 2017, **1**, 414–430.

40 J. Wang, H. Tang, L. Zhang, H. Ren, R. Yu, Q. Jin, J. Qi, D. Mao, M. Yang and Y. Wang, *Nat. Energy*, 2016, **1**, 16050.

41 J. C. Zheng, Z. Yang, Z. J. He, H. Tong, W. J. Yu and J. F. Zhang, *Nano Energy*, 2018, **53**, 613–621.